

Article

# Effects of EMS Induced Flow on Solidification and Solute Transport in Bloom Mold

Qing Fang, Hongwei Ni \*, Bao Wang, Hua Zhang and Fei Ye

The State Key Laboratory of Refractories and Metallurgy, Wuhan University of Science and Technology, Wuhan 430081, China; qfang525@sina.com (Q.F.); wangbao1983@wust.edu.cn (B.W.); huazhang@wust.edu.cn (H.Z.); yefeishangnan@163.com (F.Y.)

\* Correspondence: nihongwei@wust.edu.cn; Tel.: +86-27-6886-2811

Academic Editor: Mohsen Asle Zaeem

Received: 13 December 2016; Accepted: 17 February 2017; Published: 24 February 2017

**Abstract:** The flow, temperature, solidification, and solute concentration field in a continuous casting bloom mold were solved simultaneously by a multiphysics numerical model by considering the effect of in-mold electromagnetic stirring (M-EMS). The mold metallurgical differences between cases with and without EMS are discussed first, and then the solute transport model verified. Moreover, the effects of EMS current intensity on the metallurgical behavior in the bloom mold were also investigated. The simulated solute distributions were basically consistent with the test results. The simulations showed that M-EMS can apparently homogenize the initial solidified shell, liquid steel temperature, and solute element in the EMS effective zone. Meanwhile, the impingement effect of jet flow and molten steel superheat can be reduced, and the degree of negative segregation in the solidified shell at the mold corner alleviated from 0.74 to 0.78. However, the level fluctuation and segregation degree in the shell around the center of the wide and narrow sides were aggravated from 4.5 mm to 6.2 mm and from 0.84 to 0.738, respectively. With the rise of current intensity the bloom surface temperature, level fluctuation, stirring intensity, uniformity of molten steel temperature, and solute distribution also increased, while the growth velocity of the solidifying shell in the EMS effective zone declined and the solute mass fraction at the center of the computational outlet ( $z = 1.5$  m) decreased. M-EMS with a current intensity of 600 A is more suitable for big bloom castings.

**Keywords:** continuous casting mold; flow pattern; solidification; solute transport; electromagnetic stirring

## 1. Introduction

Most defects affecting steel quality in the continuous casting (CC) process are associated with metallurgical behavior in the mold including flow pattern, heat transfer, initial solidification, and solute transport etc. At present, in-mold electromagnetic stirring (M-EMS) used to optimize molten steel flow is a widely accepted technique in big bloom casting, which has been proved to be beneficial to enhance the columnar-to-equiaxed transition during solidification and reduce the surface and subsurface defects [1–3]. Geng et al. [4] and Yu et al. [5] indicated that the EMS parameters affects the metallurgical behavior and the steel quality significantly, an optimum EMS parameter for a certain bloom should be proposed for a higher quality. Recently, numerous mathematical and experimental studies on the CC process involving M-EMS were conducted to investigate the flow field distribution of molten steel [6–9], and the heat transfer and initial solidification behaviors influenced by EMS induced fluid flow were also studied in past years [10–13]. Yang et al. [10] and Ren et al. [13] recently discussed the effects of EMS parameters on the flow pattern and initial solidification in the big bloom mold fed by a normal nozzle with a single outlet, and stated that M-EMS can promote superheat dissipation and enhance the percentage of the equiaxed zone, while the mutual effect between the EMS induced flow and the growth of the solidifying shell lacked discussion. Sun et al. [14] who

designed a swirling flow nozzle for round bloom, concluded that a horizontal swirling flow in the mold can eliminate the superheat and depress local shell thinning. However, the solute transport phenomena associated with the EMS induced turbulent flow during the initial solidification process in the bloom mold has been rarely reported, although this deeply affects the macrosegregation profile of the final products. Aboutalebi et al. [15] and Yang et al. [16] developed a fully coupled flow, heat and solute transport model which predicted a turbulent flow induced solidification and segregation profile for CC round bloom and slab, respectively, while the relation of flow and segregation profile was not clearly explained and the effect of M-EMS was ignored. Lei et al. [17] and KwanGu et al. [18] preliminarily investigated the flow, solidification, and solute transport in CC slab mold with an electromagnetic brake, but without detailed explanation of the effect of the electromagnetic field on the solidification process and solute transport, while the verification of the solute transport model was neglected. Sun et al. [19] studied the effect of a swirling flow nozzle (SFN) on the flow, solidification, and macrosegregation behavior of casting blooms, and concluded that the formation of positive and negative segregation in the initial solidified shell can contribute to the flotation of solute-richer molten steel and the “solute washing effect” [20], which could offer the reader useful enlightenment for analyzing the swirling flow induced macrosegregation in the CC mold. However, the effects of M-EMS parameters on the macro-transport phenomena in CC bloom mold, especially the solute transport behavior, need detailed investigation.

In order to gain a deep insight into the M-EMS effects, the flow, temperature field, solidification behavior, and solute concentration field in the CC bloom mold of U71Mn steel were solved simultaneously by a three-dimensional multiphysics numerical model by considering the electromagnetic stirring force. In this paper, the metallurgical effects with EMS on the flow, level fluctuation, heat transfer, initial solidification, and solute transport phenomena in the CC mold were discussed first, and compared to that without EMS. The simulated segregation profiles of solute element carbon (C) in the region of initial solidified shell with a thickness of 30 mm at both the wide and the narrow sides were examined by the infrared carbon-sulfur determinator. Furthermore, the influences of EMS current intensity on the mold metallurgical behavior were also investigated and an optimized current intensity was suggested for big bloom casting.

## 2. Model Descriptions

### 2.1. Basic Assumptions

A three dimensional coupled model was established by combining electromagnetism, fluid flow, heat, and solute transport based on the following assumptions:

- (1) The transport phenomena in the mold are assumed to be at steady state and the influence of inclusions on the fluid flow, heat transfer, and species transport is neglected to simplify the simulation.
- (2) The impact of fluid flow on the internal heat transfer of molten steel is ignored in this model, and the liquid steel is assumed to be an incompressible Newtonian fluid. The influence of mold oscillation and mold taper on the fluid flow is also ignored.
- (3) The effect of thermal contraction on the fluid flow and temperature field in the bloom is neglected.
- (4) The mold arc is neglected, and the computational zone is assumed to be a vertical model.
- (5) The effect of the melt flow on the electromagnetic field is ignored due to the small magnetic Reynolds number (about 0.01) in the stirring process.

### 2.2. Governing Equations

#### 2.2.1. Turbulent Flow

The melt flow pattern in the mold is numerically simulated by solving the continuity and momentum equations under turbulent conditions:

$$\frac{\partial(\rho u_i)}{\partial x_i} = 0 \quad (1)$$

$$\rho \frac{\partial u_i u_j}{\partial x_j} = \frac{\partial}{\partial x_j} \left[ \mu_{\text{eff}} \left( \frac{\partial u_i}{\partial x_j} + \frac{\partial u_j}{\partial x_i} \right) \right] - \frac{\partial P}{\partial x_i} + \rho g_i + F_B + F_E + S_P \quad (2)$$

where  $\mu_{\text{eff}}$  is the effective viscosity coefficient, which is the sum of the laminar ( $\mu_l$ ) and turbulent ( $\mu_t$ ) viscosity.  $\mu_t$  can be defined as:

$$\mu_t = \rho \times f_\mu \times C_\mu \times \frac{K^2}{\varepsilon} \quad (3)$$

where  $K$  and  $\varepsilon$  are the turbulent kinetic energy and dissipation rate of this energy, respectively. The low-Reynolds number  $K$ - $\varepsilon$  turbulent model [21,22] is applied to describe the turbulence flow and solidification phenomena in the computational domain. The empirical constants are set as  $C_\mu = 0.09$  and  $f_\mu = \exp \left[ \frac{-3.4}{\left(1 + \frac{0.05K^2}{50\varepsilon}\right)^2} \right]$ , respectively.

The last term in Equation(2) accounts for the phase interaction force within the mushy zone, and it can be described by Darcy's law, the permeability  $K_p$  is presented as follows [23]:

Permeability parallel to primary dendrite arms:

$$K_p^{\text{par}} = \begin{cases} f_l < 0.7, & [4.53 \times 10^{-4} + 4.02 \times 10^{-6}(f_l + 0.1)^{-5} \cdot \frac{\lambda_2^2 \cdot f_l^3}{1-f_l}] \\ f_l \geq 0.7, & 0.07425 \cdot \lambda_1^2 [-\ln(1-f_l) - 1.487 + 2(1-f_l) - 0.5(1-f_l)^2] \end{cases} \quad (4)$$

Permeability perpendicular to primary dendrite arms:

$$K_p^{\text{per}} = \begin{cases} f_l < 0.7, & 0.00173 \times \left(\frac{\lambda_1}{\lambda_2}\right)^{1.09} \times \frac{\lambda_2^2 \cdot f_l^3}{(1-f_l)^{0.749}} \\ f_l \geq 0.7, & 0.03978 \cdot \lambda_1^2 [-\ln f_s - 1.476 + 2f_s - 1.774f_s^2 + 4.076f_s^3] \end{cases} \quad (5)$$

$$S_p = \frac{\mu_t}{K_p} (u_i - u_{s,i}) \quad (6)$$

where  $\lambda_1, \lambda_2$  are the primary arm space and secondary arm space respectively;  $u_{s,i}$  is the velocity of solid in the direction of  $i$ ;  $f_l$  is the local liquid fraction.

The source term  $F_B$  in the momentum equation represents the full buoyancy force which includes the solutal buoyancy and the thermal buoyancy effect. The detailed information is described by the following equation.

$$F_B = \rho \times g \times \beta_t \times (T - T_l) + \sum_i \rho \times g \times \beta_{C_i} \times (C_{l,i} - C_{l,0}^i) \quad (7)$$

where  $T_l$  is liquidus temperature,  $C_{l,i}$  is locally averaged concentration of solute element  $i$  in liquid phase, and  $C_{l,0}^i$  is solute concentration at the liquidus temperature. The density  $\rho$  is assumed to be a constant except in the buoyancy terms according to the Boussinesq approximation [24].

## 2.2.2. Heat Transfer Model

To obtain a precise prediction of the temperature field and solidification behavior, the enthalpy equation is employed.

$$\rho u_i \frac{\partial H}{\partial x_i} = - \frac{\partial}{\partial x_i} \left[ \left( k_l + \frac{\mu_t}{Pr_t} \right) \frac{\partial H}{\partial x_i} \right] \quad (8)$$

where  $u_i$  represents fluid flow velocity in direction of  $i$ , the turbulent Prandtl number  $Pr_t$  is set to be 0.9 [25], the total enthalpy  $H$  can be obtained by the following equation:

$$H = h_{\text{ref}} + \int_{T_{\text{ref}}}^T c_p dT + f_l L \quad (9)$$

where  $c_p$  is specific heat,  $L$  is latent heat, and liquid fraction  $f_l$  is updated by:

$$f_l = \frac{T - T_s}{T_l - T_s} (T_s < T < T_l) \quad (10)$$

$$T_l = T_{\text{pure}} - \sum_i m_i \times C_{l,i}, T_s = T_{\text{pure}} - \sum_i m_i \times C_{l,i}/k_i \quad (11)$$

$$k_i = C_{s,i}^*/C_{l,i}^* \quad (12)$$

where  $T_l$  and  $T_s$  are the liquidus and solidus temperature, respectively;  $T_{\text{pure}}$  is the fusion temperature of pure iron,  $m_i$ ,  $k_i$  are the slope of liquidus line and equilibrium partition coefficient of solute element  $i$ , respectively.  $C_{s,i}^*$  and  $C_{l,i}^*$  are the interface concentration of solute element  $i$  in the solid and liquid phase, respectively.

### 2.2.3. Solute Transport Model

The conservation equation for multicomponents in the CC system is expressed as:

$$\frac{\partial(\rho u_i c)}{\partial x_i} = \frac{\partial}{\partial x_i} \left[ \left( \frac{\mu_l}{S_{c_l}} + \frac{\mu_t}{S_{c_t}} \right) \frac{\partial c}{\partial x_i} \right] + S_c \quad (13)$$

where  $S_{c_l} = \frac{\mu_l}{\rho D_l}$  and  $S_{c_t} = 1$  [15] represent the laminar and turbulent Schmidt numbers, respectively.  $D_l$  is the liquid diffusive coefficient.  $S_c$  is the source term:

$$S_c = \frac{\partial}{\partial x_i} \left[ \rho f_s D_s \frac{\partial(c_s - c)}{\partial x_i} \right] + \frac{\partial}{\partial x_i} \left[ f_l \left( \frac{\mu_l}{S_{c_l}} + \frac{\mu_t}{S_{c_t}} \right) \right] \frac{\partial(c_l - c)}{\partial x_i} - \frac{\partial}{\partial x_i} \rho(c_l - c)(u_i - u_{i,s}) \quad (14)$$

where  $D_s$  is the solid diffusive coefficient,  $c_s$  and  $c_l$  are the species mass fraction in the solid and liquid steel, respectively.

### 2.2.4. Electromagnetism Model

For the source term in Equation (2),  $F_E$  represents the electromagnetic force, which contains radial force ( $\bar{F}_r$ ) and tangential force ( $\bar{F}_\theta$ ) [26]:

$$\bar{F}_r = -\frac{1}{8} B_0^2 \sigma^2 \left( 2\pi f - \frac{V_\theta}{r} \right)^2 \mu_0 r^3 \quad (15)$$

$$\bar{F}_\theta = \frac{1}{2} B_0^2 \sigma \left( 2\pi f - \frac{V_\theta}{r} \right) r \quad (16)$$

where  $B_0$  is the magnetic induction density at the boundary of molten steel;  $\sigma$  is the electrical conductivity of liquid steel;  $f$  is the current frequency of the EMS;  $V_\theta$  is the tangential velocity;  $\mu_0$  is the magnetoconductivity;  $r$  is the value of radial displacement. The radial force ( $\bar{F}_r$ ) is ignored for  $\bar{F}_r$  is much smaller than  $\bar{F}_\theta$  in a rotating magnetic field. The electromagnetic force is added into FLUENT by user defined functions as a momentum source. The distribution of electromagnetic intensity in the mold at the axis under different current intensity is measured by the Gauss meter, the result is presented in Figure 1.

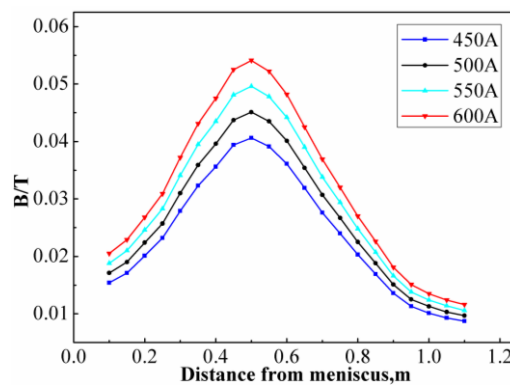


**Figure 1.** Measured distribution of electromagnetic intensity in the mold under different current intensity.

### 2.2.5. VOF Model

The steel/slag interface fluctuation in the mold is tracked by the volume fraction of fluid (VOF) method, which can track the shape of the fluctuating steel/slag interface. The detailed information and equations on the VOF model in representing the movement of the mold slag layer can be found elsewhere [27].

## 3. Simulation Procedure and Verification

The fluid flow, heat, initial solidification behavior, and solute transport in the CC bloom mold were calculated using FLUENT 15.0. The segregation profiles of C in the region of the initial solidification shell at both the wide and the narrow face were measured by an infrared carbon-sulfur determinator and compared with the calculation results.

### 3.1. Operating Condition and Parameters

The target chemical composition of U71Mn steel in the plant is listed in Table 1. The construction and installation method of submerged entry nozzle (SEN) for bloom casting is presented in Figure 2, where the immersion depth is 210 mm and the port downward angle is 15°, respectively. SEN has been proved to be a practical design in optimizing the fluid and heat transfer in the mold while producing U71Mn steel [28]. Table 2 lists the industrial conditions for producing the steel, and the thermo-solutal and physical parameters of U71Mn steel are presented in Table 3.

**Table 1.** Target chemical composition of U71Mn steel.

Chemical Composition	C	Si	Mn	P	S	Cr	Mo	Ni	Cu
Mass%	0.73	0.25	1.2	≤0.02	≤0.02	≤0.15	≤0.02	≤0.10	≤0.15

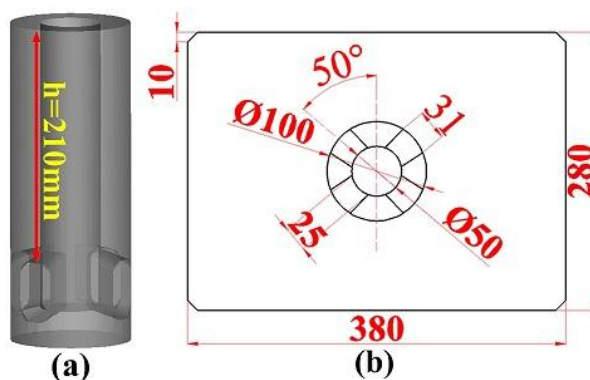


**Figure 2.** The three-dimensional view (a) and installation method (b) of submerged entry nozzle (SEN).

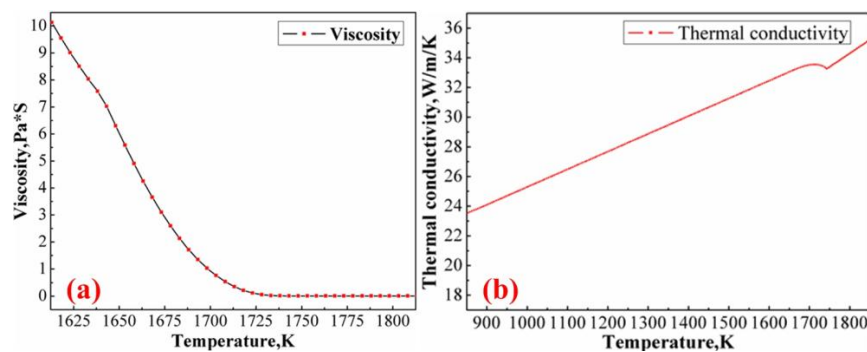
**Table 2.** Industrial conductions for U71Mn steel.

Parameters	Value
Cross section of bloom, mm <sup>2</sup>	380 × 280
Casting speed, m/min	0.63
Casting temperature, K	1765
Nozzle adaption	Figure 2
Calculation length, mm	1500
Running current of M-EMS, A	450–600
Running frequency of M-EMS, Hz	2.0
EMS center(distance from meniscus), mm	420
Height of EMS, mm	480
Water quantity in mold, L/min	2600

**Table 3.** Thermo-solutal and physical parameters of U71Mn steel.

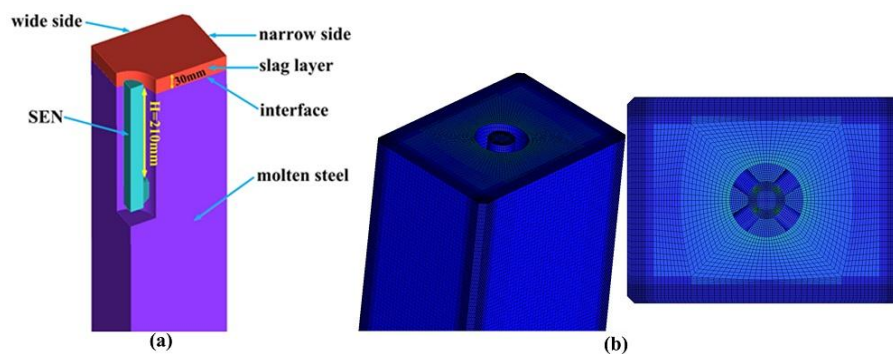
Parameters	Value
Operation density, kg/m <sup>3</sup>	7020
Latent heat, J/kg	272,000
Specific heat of liquid, J/(kg·K)	810
Specific heat of solid, J/(kg·K)	682
Electric conductivity, S/m	$7.14 \times 10^5$
Viscosity, Pa·s	Figure 3a
Thermal conductivity, W/(m·K)	Figure 3b
Diffusion coefficient of liquid, cm <sup>2</sup> /s	$0.0052 \exp\left(\frac{-11700}{8.314 \cdot T}\right)$
Diffusion coefficient of solid, cm <sup>2</sup> /s	$0.0761 \exp\left(\frac{-134557}{8.314 \cdot T}\right)$
Equilibrium partition coefficient	0.4
Slope of liquidus line	78

Viscosity and thermal conductivity are very important thermo-physical parameters for predicting the flow and solidification behavior of the steel, especially the mushy zone. The variations of viscosity and thermal conductivity with local temperature for U71Mn steel shown in Figure 3, which are calculated by the code JMatPro7.0, were applied in the calculation process.

**Figure 3.** Variations of viscosity (a) and thermal conductivity (b) with local temperature.

### 3.2. Model Building

A quarter of the three-dimensional (3D) schematic sketch of the top part of a real mold is given in Figure 4a. To simulate the behavior of the initial solidified shell more accurately, the technology of local grid refinement is applied, the meshes of FLUENT computational domain include non-uniform grids with cells about 3,100,000. The meshed geometrical model for the computational domain is presented in Figure 4b. The meshed computational model has the same geometrical parameters as the real caster.

**Figure 4.** The schematic sketch of mold and meshed model of computational domain. (a) mold top part; (b) meshed model.

### 3.3. Initial and Boundary Conditions

The initial and boundary condition for velocity, temperature, turbulent kinetic energy, dissipation rate, and species concentration are set as follows:

For computational inlet,  $v_z = v_{in} = v_{cast} \times \frac{S_{mold}}{S_{SEN}} = 0.5679$  m/s,  $v_x = v_y = 0$ ,  $k_{in} = 0.01v_{in}^2$ ,  $\varepsilon = k_{in}^{1.5}/D$ ,  $T_{in} = 1765.15$  K, and  $C_{in} = C_0 = 0.7246\%$ .  $k_{in}$  and  $\varepsilon$  are calculated by the semiempirical equations [29]. For outlet, the fully developed flow condition is adopted, where the normal gradients of all variables are set to zero. For the free surface, the normal derivative of all variables is set to be zero, and the adiabatic condition is adopted for the free surface.

For bloom wall, the detailed boundary conditions for heat transfer at the bloom wall are presented as:

In the mold region, the average heat flux is applied to describe the heat exchange effect in the actual domain [30]:

$$\bar{q} = \frac{\rho_w \times c_w \times W \times \Delta T}{S} \quad (17)$$

where  $\bar{q}$  is the average heat flux density, W/m<sup>2</sup>;  $\rho_w$  is the water density, kg/m<sup>3</sup>;  $c_w$  is the specific heat capacity of the cooling water, J/(kg·K);  $W$  is the water flow rate, m<sup>3</sup>/s;  $\Delta T$  is the water temperature difference between in and out, K;  $S$  is the effective contact area of the steel and the mold wall, m<sup>2</sup>. A correction factor ( $\alpha$ ) is necessary while calculating the solidification behavior at the bloom mold corner.

$$\bar{q}_g = \alpha \times \bar{q} \quad (18)$$

The heat transfer coefficient in the secondary cooling zone I is calculated by the following equation, in which water cooling is applied.

$$h = \beta \times 581w^{0.541}(1 - 0.0075T_w) \quad (19)$$

where  $h$  is the heat transfer coefficient, W/(m<sup>2</sup>·K);  $w$  is the water density, L/(m<sup>2</sup>·s); and  $T_w$  represents the ambient temperature;  $\beta$  is the correction factor.

### 3.4. Verification of Solute Transport

To validate the mathematical coupled model, the mass fraction of the chemical element C in the initial solidified shell thickness of 30 mm is evaluated by an infrared carbon-sulfur determinator. The specific locations of the drilling samples are presented in Figure 5. Where the samples are drilled with a 4.2 mm diameter drill up to a depth about 20 mm and the weight is around 2 g. The test and simulated results for the verification are without EMS.

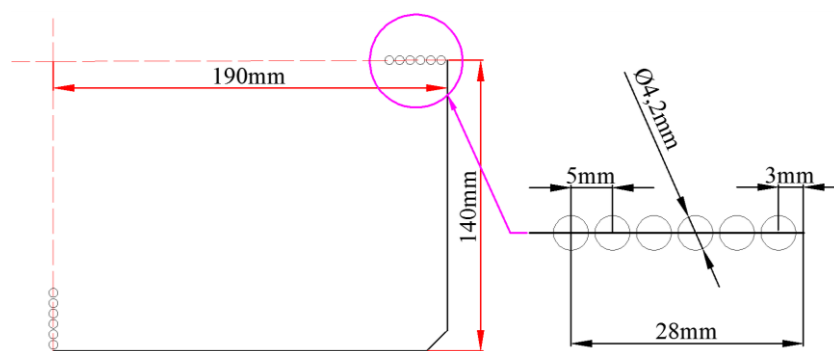
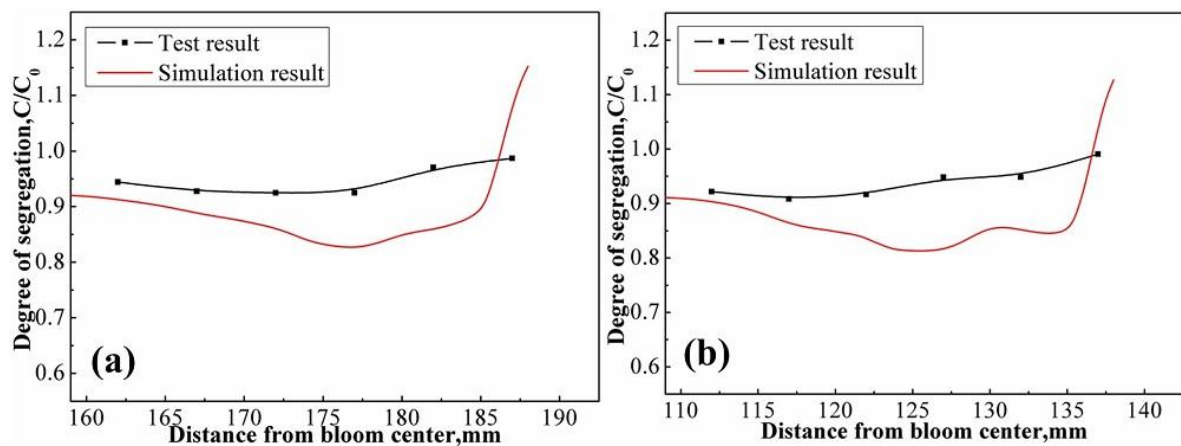


Figure 5. Distributions of drilling samples in the initial solidified shell.

Figure 6 shows the comparison between the simulation results and the result from the infrared carbon-sulfur determinator. A basically consistent variation tendency can be observed between the simulation results and testing results along both width direction and thickness direction.



**Figure 6.** Comparison between measured and simulated segregation profiles of C in the region of initial solidification shell. (a) width direction; (b) thickness direction.

## 4. Results and Discussion

### 4.1. Metallurgical Effects of M-EMS

Two simulation cases in this paper are discussed first and compared to find out the exact effect of mold EMS on flow, heat transfer, initial solidification, and solute transport in the mold region. One is the case without EMS, the other is the case loaded with EMS, in which the current intensity is 600 A and the electromagnetic frequency is 2.0 Hz.

#### 4.1.1. Flow Field

Figure 7 shows the contour and vector of flow patterns in the upper part of the bloom without EMS (a) and with EMS (b). Also, the velocity contour of several key cross sections in the mold zone for the two cases is presented in Figure 7, which are  $z = 0.234$  m for the center of the SEN outlets,  $z = 0.42$  m for the EMS center and  $z = 0.7$  m for the mold outlet, respectively. In the bloom mold without EMS, the bulk flow leaving the SEN outlets impinges on the mold corner wall and is split into two opposing directions. Upper circulation is confined by the walls and meniscus and the lower circulation is formed by the mold corner and the return flow near the mold center. The center of the upper circulation is located at around 0.09 m bloom from the meniscus, and the lower circulation center is locating at approximately 0.45 m. When the mold is loaded with EMS, four obvious circulations are formed upon and under the EMS center, the two lower circulations can improve the heat transfer mechanism of molten steel in the EMS effect area, eliminate steel superheat, and promote uniform growth of the solidifying shell. The location of the upper circulation center in the diagonal plane changes to 0.21 m, with a higher velocity than the case without EMS, but the circulation under the nozzle outlets is eliminated and the flow is changed to the casting direction because of the increasing stirring effect of the EMS. In the center cross section of the SEN outlets, the four jet flows impinge on the mold corner, rebound to the bloom center and form four horizontal circulations near the narrow sides with a high velocity around the mold corner without EMS. The horizontal circulations remain for a while, then are eliminated at the mold outlet. The horizontal circulations created by the mold wall and molten steel in the bloom center can be changed into a strong horizontal swirling flow gradually by EMS, and the strongest flow occurs in the cross section of the EMS center. In the horizontal swirling flow, the largest tangential velocity locates at the solidification front near the center of the wide and narrow sides. The strong tangential velocity can affect the solidification behavior in the mold, effectively prevent the growth of columnar crystal, promote the growth of equiaxed grain [31], and be beneficial to the homogeneity of temperature and solute element in the molten steel.

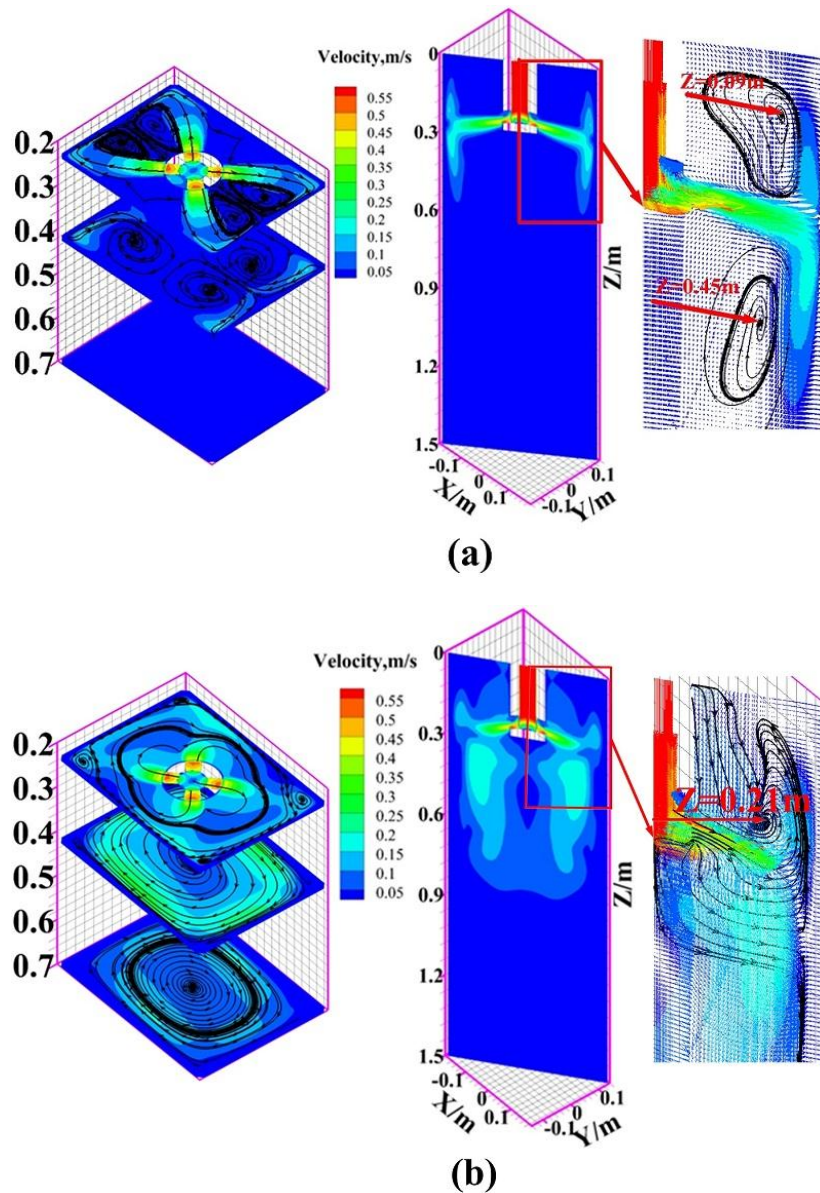


**Figure 7.** Velocity contour and vector in the upper part of the mold for the cases without (a) and with (b) electromagnetic stirring (EMS).

The comparison of the three-dimensional time-averaged level fluctuation with and without EMS is presented in Figure 8. The height difference between the zenith and the nadir of the free surface level is defined as the largest level fluctuation value of the mold. The largest level fluctuation value without EMS is about 4.5 mm, which happens at very few positions, for most of the other places the level fluctuation is less than 1 mm, the free surface is relatively stable. After the EMS is loaded, the level fluctuation at the center and edge of the free surface in the mold moves up and down respectively, which is affected by the electromagnetic force at the upper mold. The largest value of level fluctuation is 6.2 mm in the case with EMS. For bloom castings, the value of level fluctuation should be controlled as low as possible while the M-EMS can aggravate the movement of mold flux, which will increase the chance of slag entrapment. A favorable electromagnetic stirring effect along with a relatively stable free surface should be obtained to guarantee proper metallurgical behavior.

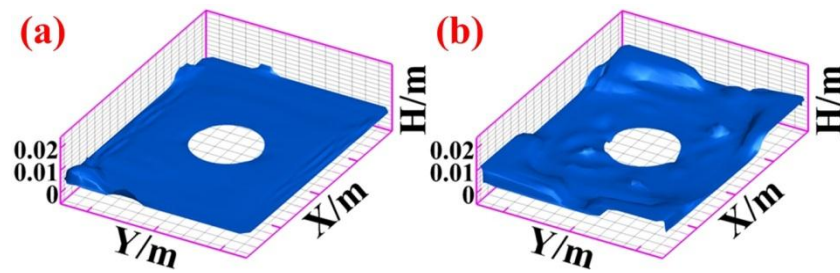


Figure 8. Comparison of three dimensional level fluctuations in the mold without (a) and with (b) EMS.

#### 4.1.2. Heat Transfer and Solidification

Figure 9 presents the temperature contour at the diagonal plane ((a) without EMS, (b) 600 A, 2.0 Hz) and the temperature distribution of molten steel at the computational centerline for the two cases (c). The temperature at the molten steel core without EMS rapidly decreases from 1765 K to 1735.7 K at 0.3 m below the meniscus, and with little change in the rest of the computational zone, at which the centerline temperature decreases from 1735.7 K at 0.3 m below the meniscus to 1728 K at the computational outlet. While the temperature at the liquid core at 0.3 m below the meniscus is 1737 K after the EMS is loaded, the average temperature in the molten steel between 0.3 m and 0.48 m below the meniscus is higher than the case without EMS, and the temperature decreases from 1735.2 K at 0.48 m below the meniscus to 1725.4 K at the computational outlet. The temperature of molten steel with EMS is uniformly distributed and remains at around 1725 K from 0.8 m to 1.5 m below the meniscus, while the molten steel temperature without EMS is non-uniformly distributed and remains in remarkable decline at about 2.6 K higher at the center of the computational outlet. Therefore, the mold EMS can effectively reduce and even eliminate the superheat of the molten steel by retaining the molten steel at a high temperature in the upper zone of the mold.

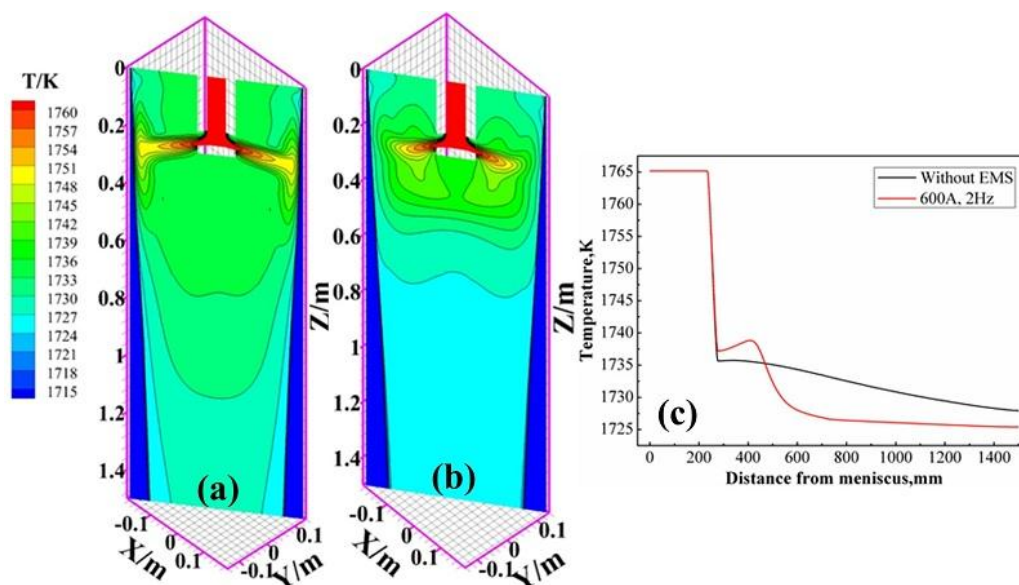
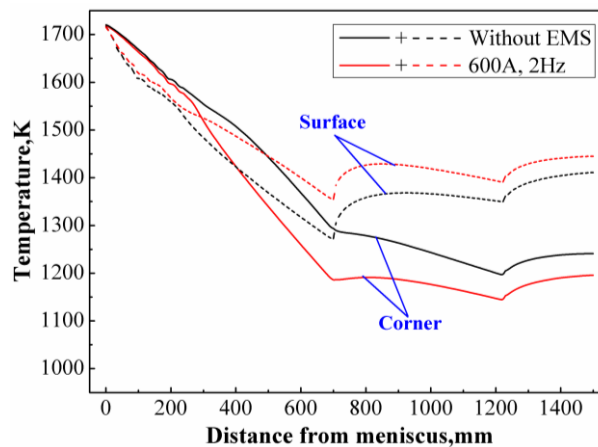


Figure 9. Temperature contour at the diagonal planes ((a) without EMS; (b) 600 A, 2.0 Hz) and molten steel temperature at computational centerline (c) for the two cases.

Figure 10 shows the temperature variation at the centerline of the bloom wide face and chamfered corner in the two cases, in which the solid and dashed lines represent the corner and surface temperature, respectively. The variation rule of temperature at both the bloom surface and the corner with and without can be easily understood by combining the flow results mentioned above.

The surface and corner temperature at 0–0.2 m below the meniscus is almost the same in the two cases because of the small EMS effect in this region. In the EMS effect area, the descent velocity of the mold corner temperature in the case loaded with EMS is larger than the other one, because the electromagnetic force can apparently lighten the scouring effect of the jet flow on the corner wall and accelerate the heat transfer process of the corner. The corner temperatures at the mold outlet in these two cases are 1286 K and 1180 K, respectively, and the temperature difference decreases gradually as the casting process continues, which is changed to 1241 K and 1195 K at the computational outlet, respectively. The corner temperature changes about  $\pm 30$  K till the bloom reaches to the straightening area, which effectively avoids the high-temperature brittle zone of the steel and prevents the chance of transverse cracks. The surface temperature in the EMS effective zone is higher than the case without EMS, because the horizontal swirling flow generated by EMS can strongly move the solidification front into the bloom center, then the solidification front is replaced by high temperature molten steel. The bloom surface temperature increases with the change of the cooling condition, which increases from 1272 K at the mold outlet to 1411 K at the computational outlet without EMS and from 1355 K to 1440 K with EMS, respectively. The values of temperature rise are 136 K without EMS and 85 K with EMS, which indicates that EMS in the bloom mold can reduce the possibility of surface cracks.



**Figure 10.** Temperature variations at the centerline of the bloom wide face and chamfered corner.

Figure 11 shows the liquid fraction distributions at the diagonal plane and cross section of the EMS center ( $z = 0.42$  m) for the two different cases. The growth velocity of the solidifying shell at the mold corner in the impact area in the case without EMS is lower than the other because of a remarkable impingement of the jet flow on the corner wall, and the solidified shell thickness at the corner of the computational outlet is apparently thinner. Compared with the case without EMS, the solidified shell in the cross section  $z = 0.42$  m in the case loaded with EMS is thicker at the corner, but thinner at both the wide and narrow sides, and the solidified shell distribution is more uniform.

Figure 12 presents the shell thickness and liquid/solid distributions at the  $y$ - $z$  plane ( $x = 0$  m) along the casting direction for the two cases, where the solid line refers to the case without EMS, while the dashed line represents the case loaded with EMS. The growth rhythm of the solidifying shell in the width direction is associated with the results shown in Figure 11, the growth velocity of the solidifying shell at the narrow side in the case loaded with EMS is slower in the EMS effective zone and the shell thickness at the mold outlet ( $z = 0.7$  m) is 14.2 mm, which is about 3 mm thinner than the case without EMS. With the decrease of electromagnetic force, the shell thickness difference between the two cases decreases as well, the solidified shell at the computational outlet for the two cases is 26.86 mm with EMS and 28.3 mm without EMS, respectively. The difference in mushy zone length variation between the case with and without EMS can also be observed in Figure 12, in which the length of the mushy zone under the EMS effective zone is significantly smaller, especially in the EMS center, where the mushy zone lengths are 3.25 mm and 5.4 mm respectively. The main reason for the difference in mushy

zone length is the remarkable tangential velocity at the solidification front of the narrow side, which is generated by the electromagnetic force. M-EMS can reduce the growth velocity of the solidifying shell and the length of the mushy zone in the EMS effective zone, which makes the shell thickness at the computational outlet 1.44 mm thinner than the case without EMS.

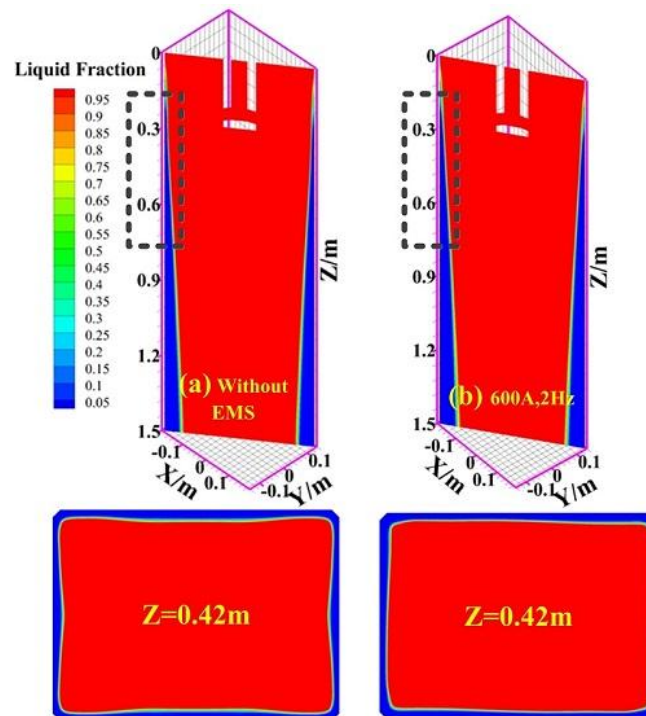


Figure 11. Liquid fraction distributions at the diagonal plane and the EMS center for different cases.

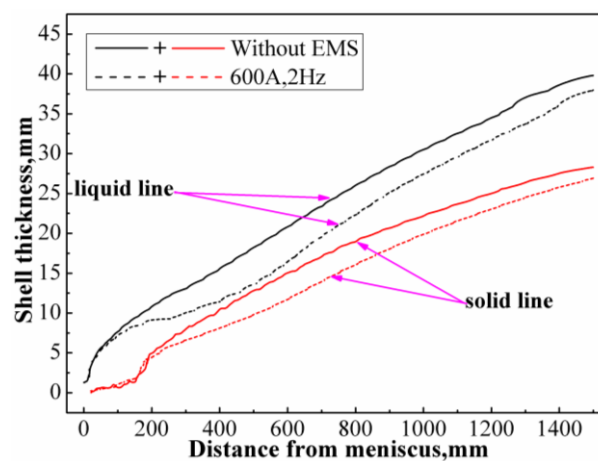


Figure 12. Liquid and solid distributions at the  $y$ - $z$  plane along the casting direction for different cases.

#### 4.1.3. Solute Transport

Figure 13 presents the distributions of solute element C on the diagonal plane ((a) the case without, (b) the case loaded with EMS) and at the diagonal line of the computational outlet(c) in the two different cases. Figure 14 shows the distributions of solute element C on the  $y$ - $z$  plane, various cross sections for the bloom ((a) without EMS, (b) 600 A, 2.0 Hz) and at the centerline of the computational outlets (c) in the two different casting cases, in which the cross sections of  $z = 0.234$  m (center cross section of SEN outlets),  $z = 0.42$  m (EMS center),  $z = 0.7$  m (mold outlet) and  $z = 1$  m are chosen to display more

intuitively the effect of EMS on the distribution of solute element C at the bloom cross section. For the case without EMS, the original liquid steel with initial mass fraction of solute element C (0.725%) is sprayed into the mold through the four outlets of SEN which are pointed directly at the mold corners, the primitive steel channels are formed by the effect of the inertia force, and the liquid steel with a high solute content floats upward to the meniscus dead zone because of the density change of liquid steel with temperature, which leads to the appearance of positive segregation in the 4 mm initial solidified shell. When arriving at the flow impact area, the impingement of liquid steel on the mold corner can dispel the enrichment of the solute at the solidification front and as there is not enough time to supply a rich solute content while the solidification continues, a negative position will be developed under this condition, and the maximum negative segregation in the diagonal plane will occur at the impact point. The high level of negative segregation is gradually reduced after the bloom is pulled out of the EMS effective zone, where the enriched solute steel will again gather at the solidification front. Compared with the result of solute element distribution at the bloom corner, a much weaker impingement effect happens around the wide and narrow sides of the bloom, the degree of negative segregation in the solidified shell of the narrow side is obviously lower. The maximum negative segregation is 0.74 when the corner solidified shell thickness is 10 mm and 0.84 when the shell thickness at the width direction is 15 mm. For the case loaded with EMS, the jet trajectory is gradually changed by the electromagnetic force, the impact pressure is lightened, and the maximum negative segregation at the bloom corner improves to 0.78 where the shell thickness is 12.5 mm compared with the case without EMS. The degree of negative segregation in the solidified shell around the wide and narrow sides in the EMS effective zone is more serious than the case without EMS, because the high tangential velocity near the solidification front around the center of the bloom narrow and wide sides can wash out the solute enriched mushy steel and move it into the bloom center, thereby enhancing the average mass fraction of the solute element C in the molten steel. The largest negative segregation at the width centerline of the computational outlet is 0.738, where the thickness is about 9.2 mm. Compared with the case without EMS, the degree and area of negative segregation in the initial solidified shell in the case loaded with EMS is larger, so the average mass fraction of solute element C in the bloom center is relatively higher due to the mass conservation law. The mass fractions of element C at the center of the computational outlet with and without EMS are 0.7904% and 0.7743%, respectively.

For big bloom castings, the main functions of M-EMS are in eliminating the superheat of the molten steel, making the temperature and solute in the molten steel uniform, improving the non-metallic inclusion floatation, promoting the ability of fluxes for adsorption of inclusion, and improving the solidification structure of the bloom. There is no obvious improvement of M-EMS on centerline segregation of big bloom casting, the effective technologies to reduce the centerline segregation for big bloom casting are soft reduction and final electromagnetic stirring [32]. In many steel plants, the combination of M-EMS with soft reduction or final EMS is widely applied to improve the internal quality of the casting bloom.

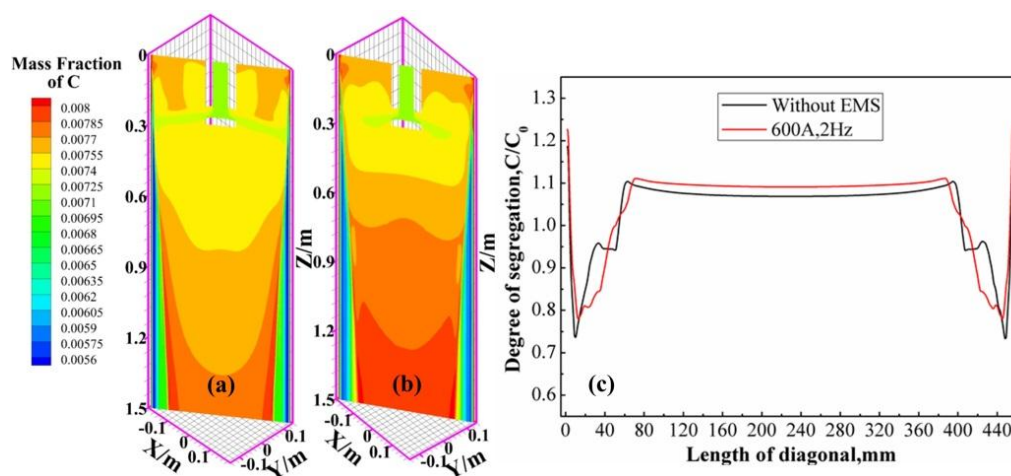


**Figure 13.** Distributions of solute element C on the diagonal plane ((a) without EMS; (b) 600 A, 2 Hz) and at the diagonal line of the computational outlets (c).

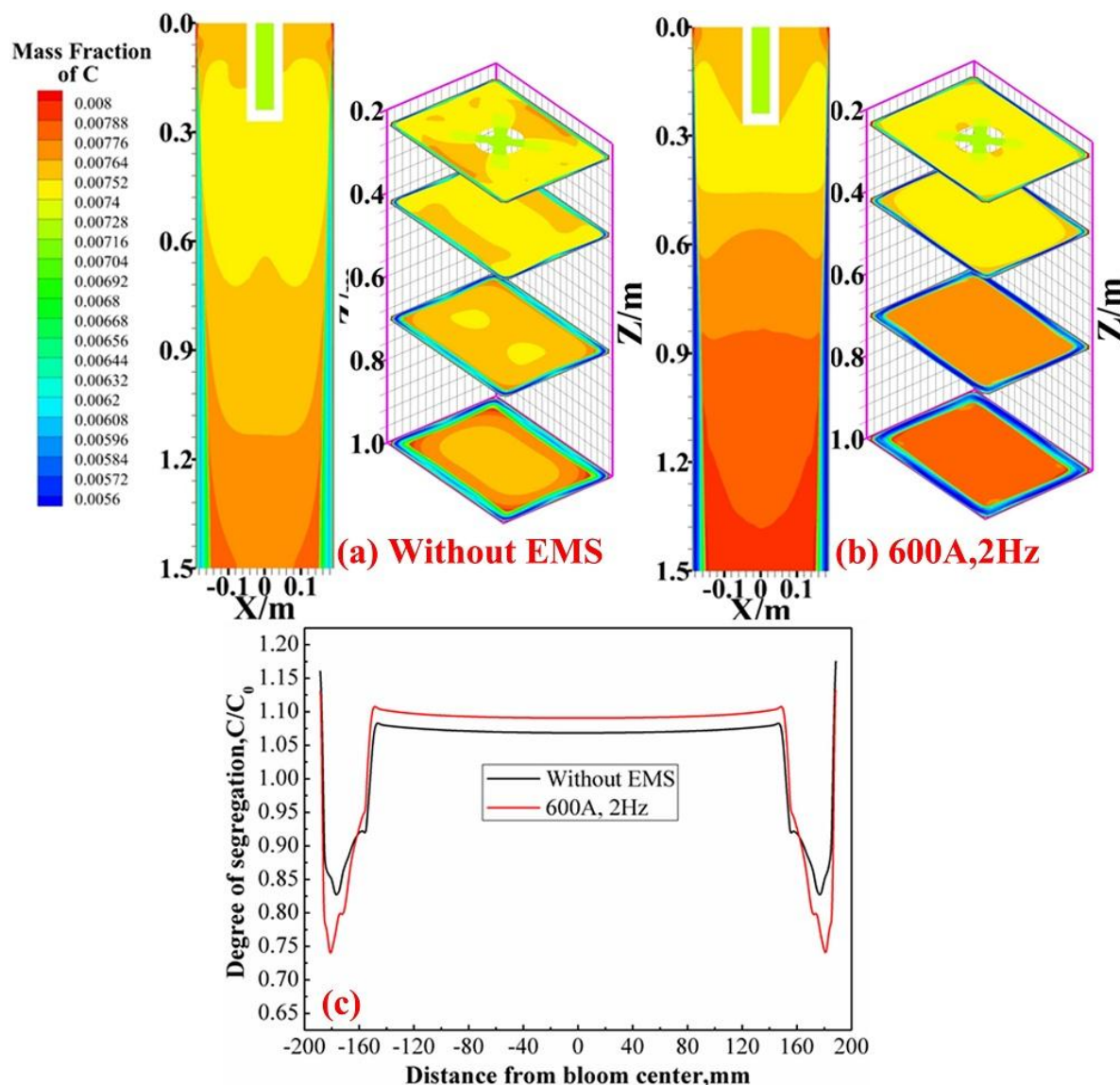


**Figure 14.** Distributions of solute element C on the  $y-z$  plane, at various cross sections of the bloom (a,b), and the centerline of the computational outlets (c).

#### 4.2. Effect of Current Intensity

After analyzing and comparing the results of the flow pattern, heat transfer, initial solidification, and solute transport in the CC bloom mold with and without EMS (600 A, 2.0 Hz), the exact effect of EMS current intensity on the metallurgical behavior in the mold will also now be discussed in this paper. The EMS parameters for the four cases are 450 A, 500 A, 550 A, and 600 A respectively, of which the frequencies are fixed at 2.0 Hz. To avoid repeating, the influence of different EMS frequencies is ignored because of the similar changing rule to current intensity.

Figure 15 presents the three dimensional level fluctuation in the mold under different current intensities. The fluctuation range of the liquid level in the mold rises with the increase of current intensity and the maximum site of the level fluctuation occurs near the four corners of the bloom, and the largest fluctuating values are 5.3 mm, 5.7 mm, 5.9 mm, and 6.2 mm, respectively. The fluctuation degree increases with the rise of current intensity. For big bloom castings, the value of level fluctuation should be controlled within around  $\pm 3$  mm, and the maximum fluctuation of the four current intensities are close to this range.

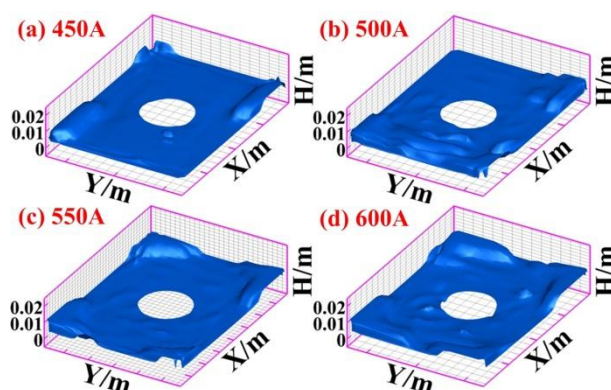


Figure 15. Comparison of three dimensional level fluctuations under different current intensity.

The velocity vector (a) and distribution of element C (b) at the cross section of EMS center ( $z = 0.42$  m) are presented in Figure 16. With the increase of current intensity, the tangential velocity at the solidification front is obviously increased, especially at the places near the center of the wide and narrow sides; the largest velocity at this moment for these four cases is 0.197 m/s, 0.219 m/s, 0.24 m/s, and 0.271 m/s respectively. The stirring effect is not satisfactory when the current intensity is less than 500 A, at which the distribution of solute element C in the cross section of the EMS center still remains part of the initial injection trajectory of the molten steel, the stirring force is not strong enough to improve the uniformity of solute and temperature in the molten steel, and the ability of inclusion flotation is not significantly enhanced. When the current intensity is larger than 500 A, the stirring effect increases with the rise of current intensity, and the distribution of solute is more and more uniform in the bloom cross section of the EMS effective zone.

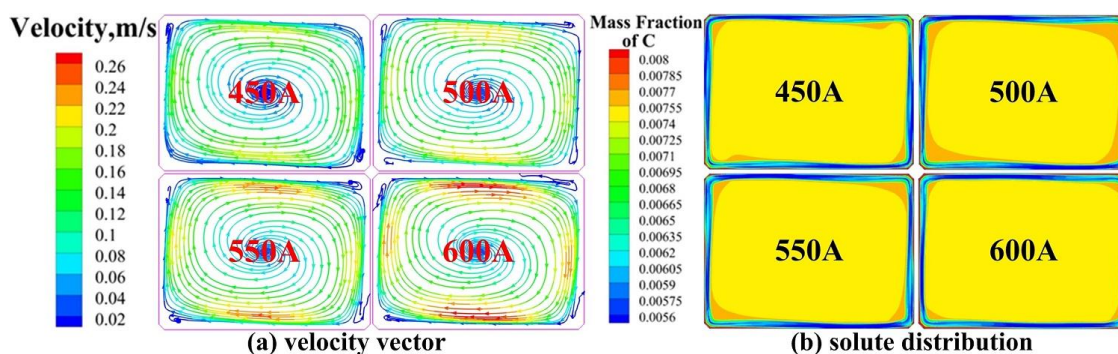
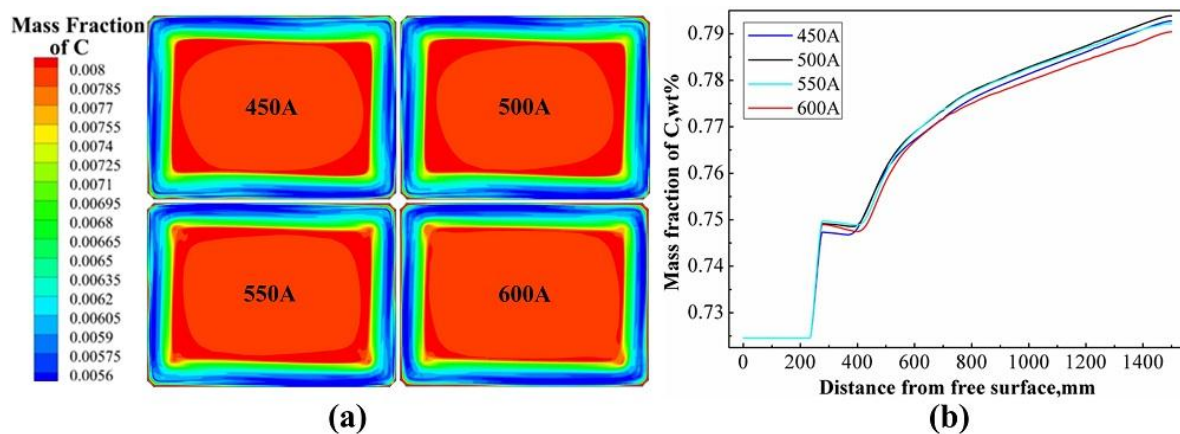


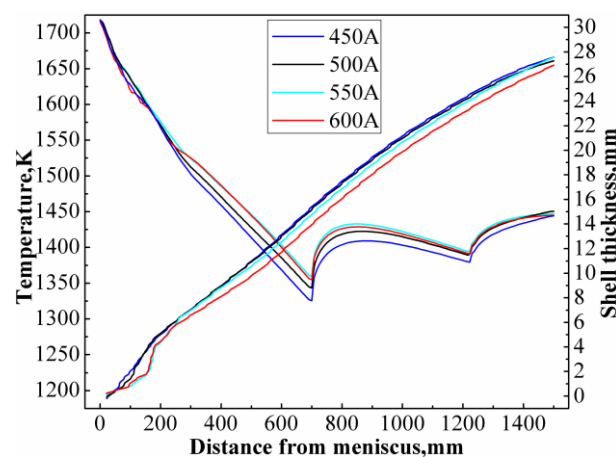
Figure 16. Velocity vector (a) and distribution of element C (b) at EMS center.

Figure 17 shows the distribution of solute element C at computational outlets (a) and the centerline along the casting direction (b) under different current intensities. It can be seen that the distribution law of the solute element in the solidified shell under different EMS current intensities is very similar, the maximum mass fraction of solute element C is presented at the solidification front, where the positive segregation will be formed in the mushy zone about to solidify. Compared with the other three cases, the area of solute enriched steel at the solidification front is smaller and the mass fraction of the solute element C at the bloom center is lower in the case with 600 A EMS. The mass fractions of C at the center of the computational outlet are 0.79275% for 450 A, 0.79389% for 500 A, 0.79214% for 550 A, and 0.79042% for 600 A, respectively.



**Figure 17.** Distribution of element C at computational outlet (a) and at centerline (b).

Figure 18 displays the variation of surface temperature and shell thickness along with casting direction at different current intensities. With the increase of current intensity (from 450 A to 550 A), the surface temperature increases as well, when the current intensity is over 550 A, the surface temperature does not result in any obvious change. The surface temperatures at the mold outlet ( $z = 700$  mm) for each case are 1325.7 K for 450 A, 1343.3 K for 500 A, 1359.4 K for 550 A, and 1355 K for 600 A, respectively. Also, 1391.5 K, 1400.9 K, 1405.8 K, and 1403.1 K at the outlet of the secondary cooling zone I ( $z = 1.23$  m), which then increase to 1444.2 K, 1450.7 K, 1447.2 K and 1445 K respectively at the computational outlet due to the change of heat transfer conditions, respectively. With the increase of current intensity, the electromagnetic force rises, while the growth velocity of the solidifying shell in the EMS effect zone decreases. The solidified shell in the thickness direction at the mold outlet at four different current intensities is about 15.3 mm for 450 A, 15.2 mm for 500 A, 14.8 mm for 550 A, and 14.2 mm for 600 A, respectively, and increases to 27.55 mm, 27.2 mm, 27.57 mm, and 26.86 mm at the outlet of computational zone ( $z = 1500$  mm), respectively.



**Figure 18.** Variation of surface temperature and shell thickness along with casting direction at different current intensities.

By comprehensively considering the mold metallurgical behavior at different current intensities, the M-EMS with a current intensity of 600 A was found to be more suitable for big bloom castings than the other cases.

## 5. Conclusions

The multi-physical metallurgical behavior in the bloom mold loaded with EMS was investigated by a three-dimensional numerical model. The effects of EMS induced flow on the heat transfer, solidification, and solute transport were studied in detail. The solute transport model was verified and metallurgical differences under different EMS conditions were discussed. The conclusions are summarized as follows:

- (1) The basically consistent variation tendency of the segregation profiles of solute element C in the region of the initial solidified shell with a thickness of 30 mm at both the wide and narrow sides can be observed between the simulated and measured results.
- (2) Compared with the case without EMS, the bloom mold loaded with EMS is beneficial to the elimination of steel superheat, reduces the breadth of the mushy zone, and aggravates the level fluctuation from 4.5 mm to 6.2 mm. The distribution of temperature, solute, and solidified shell is more uniform in the EMS effective zone, the highest degree of negative segregation at the mold corner decreases from 0.78 to 0.74, but increases from 0.84 to 0.738 at the narrow and wide sides. The mass fraction of solute element C at the computational outlet increases from 0.7743% to 0.7904%. The EMS mold is not beneficial to the improvement of centerline segregation for big bloom casting.
- (3) With the increase of EMS current intensity (from 450 A to 600 A), the stirring effect and tangential velocity at the solidification front around the center of the wide and narrow sides increases, the level fluctuation is aggravated from 5.3 mm to 6.2 mm, the surface temperature in the EMS effective zone, the uniformity degree of temperature, and the solute distribution in the molten steel all increase as well, while the growth velocity of the solidifying shell thickness in the EMS effective zone decreases. The mass fraction of solute element C at the center of the computational outlets ( $z = 1.5$  m) decreases from 0.7925% to 0.7904%. The M-EMS with a current intensity of 600 A is more suitable for big bloom castings.
- (4) The model has great application potential for a qualitative study of multi-physical phenomena in the bloom mold coupled with EMS, especially for the solute transport and solidification process coupled with turbulent flow. However, the present model would apply only to part of the caster, particularly the turbulent flow zone. To enhance the inner quality of the final products, the heat transfer and solute transport behavior below the computational domain need further investigation, especially for efficient ways to alleviate central segregation.

**Acknowledgments:** The authors would like to express their gratitude for the financial support by the National Natural Science Fund of China (51604200).

**Author Contributions:** Hongwei Ni and Hua Zhang conceived and designed the study. Qing Fang performed the experiments and simulations. Bao Wang contributed to the result analysis and paper preparation. Qing Fang and Fei Ye wrote the manuscript.

**Conflicts of Interest:** The authors declare no conflicts of interest.

## References

1. Wu, H.J.; Wei, N.; Bao, Y.P.; Wang, G.X.; Xiao, C.P.; Liu, J.J. Effect of M-EMS on the solidification structure of a steel billet. *Int. J. Miner. Metall. Mater.* **2011**, *18*, 159–164. [[CrossRef](#)]
2. Sun, T.; Yue, F.; Wu, H.J.; Guo, C.; Li, Y.; Ma, Z.C. Solidification structure of continuous casting large round billets under mold electromagnetic stirring. *J. Iron Steel Res. Int.* **2016**, *23*, 329–337. [[CrossRef](#)]
3. Jiang, D.B.; Zhu, M.Y. Solidification Structure and Macrosegregation of Billet Continuous Casting Process with Dual Electromagnetic Stirrings in Mold and Final Stage of Solidification: A Numerical Study. *Metall. Mater. Trans. B.* **2016**, *47*, 3446–3458. [[CrossRef](#)]
4. Geng, X.; Li, X.; Liu, F.B.; Jiang, Z.H. Optimisation of electromagnetic field and flow field in round billet continuous casting mould with electromagnetic stirring. *Ironmak. Steelmak.* **2015**, *42*, 675–682. [[CrossRef](#)]

5. Yu, H.Q.; Zhu, M.Y. 3-D Numerical simulation of flow field and temperature field in a round billet continuous casting mold with electromagnetic stirring. *Acta Metal. Sin.* **2008**, *44*, 1465.
6. Liu, H.P.; Xu, M.G.; Qiu, S.T.; Zhang, H. Numerical simulation of fluid flow in a round bloom mold with in-mold rotary electromagnetic stirring. *Metall. Mater. Trans. B* **2012**, *43*, 1657–1675. [[CrossRef](#)]
7. Singh, R.; Thomas, B.G.; Vanka, S.P. Large eddy simulations of double-ruler electromagnetic field effect on transient flow during continuous casting. *Metall. Mater. Trans. B* **2014**, *45*, 1098–1115. [[CrossRef](#)]
8. Singh, R.; Thomas, B.G.; Vanka, S.P. Effects of a magnetic field on turbulent flow in the mold region of a steel caster. *Metall. Mater. Trans. B* **2013**, *44*, 1201–1221. [[CrossRef](#)]
9. Timmel, K.; Eckert, S.; Gerbeth, G. Experimental investigation of the flow in a continuous-casting mold under the influence of a transverse, direct current magnetic field. *Metall. Mater. Trans. B* **2011**, *42*, 68–80. [[CrossRef](#)]
10. Yang, Z.G.; Wang, B.; Zhang, X.F.; Wang, Y.T.; Dong, H.B. Effect of electromagnetic stirring on molten steel flow and solidification in bloom mold. *J. Iron Steel Res. Int.* **2014**, *21*, 1095–1103. [[CrossRef](#)]
11. Ren, B.Z.; Chen, D.F.; Wang, H.D.; Long, M.J.; Han, Z.W. Numerical analysis of coupled turbulent flow and macroscopic solidification in a round bloom continuous casting mold with electromagnetic stirring. *Steel Res. Int.* **2015**, *86*, 1104–1115. [[CrossRef](#)]
12. Tian, X.Y.; Zou, F.; Li, B.W.; He, J.C. Numerical analysis of coupled fluid flow, heat transfer and macroscopic solidification in the thin slab funnel shape mold with a new type EMBr. *Metall. Mater. Trans. B* **2010**, *41*, 112–120. [[CrossRef](#)]
13. Ren, B.Z.; Chen, D.F.; Wang, H.D.; Long, M.J.; Han, Z.W. Numerical simulation of fluid flow and solidification in bloom continuous casting mould with electromagnetic stirring. *Ironmak. Steelmak.* **2015**, *42*, 401–408. [[CrossRef](#)]
14. Sun, H.B.; Zhang, J.Q. Effect of feeding modes of molten steel on the mould metallurgical behavior for round bloom casting. *ISIJ Int.* **2011**, *51*, 1657–1663. [[CrossRef](#)]
15. Aboutalebi, M.R.; Hasan, M.; Guthrie, R.I.L. Coupled turbulent flow, heat, and solute transport in continuous casting processes. *Metal. Mater. Trans. B.* **1995**, *26*, 731–744. [[CrossRef](#)]
16. Yang, H.L.; Zhao, L.G.; Zhang, X.Z.; Deng, K.W.; Li, W.C.; Gan, Y. Mathematical simulation on coupled flow, heat, and solute transport in slab continuous casting process. *Metal. Mater. Trans. B* **1998**, *29*, 1345–1356. [[CrossRef](#)]
17. Lei, H.; Zhang, H.W.; He, J.C. Flow, solidification, and solute transport in a continuous casting mold with electromagnetic brake. *Chem. Eng. Technol.* **2009**, *32*, 991–1002. [[CrossRef](#)]
18. Kang, K.G.; Ryou, H.S.; Hur, N.K. Coupled turbulent flow, heat, and solute transport in continuous casting processes with an electromagnetic brake. *Numer. Heat Transf. Part A* **2005**, *48*, 461–481. [[CrossRef](#)]
19. Sun, H.B.; Zhang, J.Q. Macrosegregation improvement by swirling flow nozzle for bloom continuous castings. *Metal. Mater. Trans. B.* **2014**, *45*, 936–946. [[CrossRef](#)]
20. Asai, S.; Nishio, N.; Muchi, I. Theoretical analysis and model experiments on electromagnetically driven flow in continuous casting. *ISIJ Int.* **1982**, *22*, 126–133. [[CrossRef](#)]
21. Jones, W.P.; Launder, B.E. The calculation of low-Reynolds-number phenomena with a two-equation model of turbulence. *Int. J. Heat Mass Trans.* **1973**, *16*, 1119–1130. [[CrossRef](#)]
22. Lam, C.K.G.; Bremhorst, K. A modified form of the  $k$ - $\epsilon$  model for predicting wall turbulence. *ASME Trans. J. Fluids Eng.* **1981**, *103*, 456–460. [[CrossRef](#)]
23. Poirier, D.R. Permeability of flow of interdendritic liquid in columnar-dendritic alloys. *Metal. Mater. Trans. B* **1987**, *18*, 245–255. [[CrossRef](#)]
24. Li, W.S.; Shen, B.Z.; Shen, H.F.; Liu, B.C. Modelling of macrosegregation in steel ingots: Benchmark validation and industrial application. *IOP Conf. Ser. Mater. Sci. Eng.* **2012**, *33*, 1–8. [[CrossRef](#)]
25. Hrenya, C.M.; Bolio, E.J.; Chakrabarti, D.; Sinclair, J.L. Comparison of low Reynolds number  $k$ - $\epsilon$  turbulence models in predicting fully developed pipe flow. *Chem. Eng. Sci.* **1995**, *50*, 1923–1941. [[CrossRef](#)]
26. Spitzer, K.H.; Dubke, M.; Schwerdtfeger, K. Rotational electromagnetic stirring in continuous casting of round strands. *Metall. Mater. Trans. B* **1986**, *17*, 119–131. [[CrossRef](#)]
27. Deng, A.Y.; Xu, L.; Wang, E.G.; He, J.C. Numerical analysis of fluctuation behavior of steel/slag interface in continuous casting mold with static magnetic field. *J. Iron Steel Res. Int.* **2014**, *21*, 809–816. [[CrossRef](#)]
28. Zhao, Z.F.; Ni, H.W.; Zhang, H.; Chen, G.Y.; Yi, W.; Hong, J. Technology and process optimisation of bloom casting of ultrahigh speed rail steel. *Ironmak. Steelmak.* **2014**, *41*, 539–546. [[CrossRef](#)]

29. Lai, K.Y.M.; Salcudean, M.; Tanaka, S.; Guthrie, R.I.L. Mathematical modeling of flows in large tundish systems in steelmaking. *Metall. Mater. Trans. B* **1986**, *17*, 449–459. [[CrossRef](#)]
30. Alizadeh, M.; Jahromi, A.J.; Abouali, O. A new semi-analytical model for prediction of the strand surface temperature in the continuous casting of steel in the mold region. *ISIJ Int.* **2008**, *48*, 161–169. [[CrossRef](#)]
31. Yu, H.Q.; Zhu, M.Y. Influence of electromagnetic stirring on transport phenomena in round billet continuous casting mould and macrostructure of high carbon steel billet. *Ironmak. Steelmak.* **2012**, *39*, 574–584. [[CrossRef](#)]
32. Zeng, J.; Chen, W.; Wang, Q.; Wang, G. Improving inner quality in continuous casting rectangular billets: Comparison between mechanical soft reduction and final electromagnetic stirring. *Trans. Indian Inst. Metals* **2016**, *69*, 1–10. [[CrossRef](#)]



© 2017 by the authors. Licensee MDPI, Basel, Switzerland. This article is an open access article distributed under the terms and conditions of the Creative Commons Attribution (CC BY) license (<http://creativecommons.org/licenses/by/4.0/>).